Physical Chemistry Chemical Physics c1cp22863c

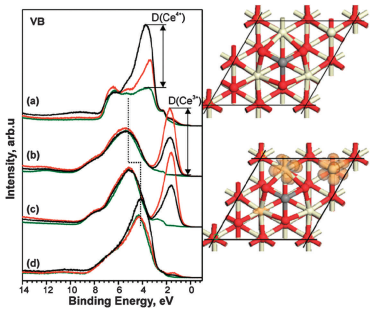

Q1 **On the interaction of Mg with the (111) and (110) surfaces of ceria**

Michael Nolan,* Yaroslava Lykhach, Nataliya Tsud, Tomáš Skála, Thorsten Staudt, Kevin C. Prince, Vladimír Matolín and Jörg Libuda*

The interaction of Mg and CeO_2 is studied with photoelectron and resonant photoelectron spectroscopy and DFT + U simulations.

Please check this proof carefully. **Our staff will not read it in detail after you have returned it.** Translation errors between word-processor files and typesetting systems can occur so the whole proof needs to be read. Please pay particular attention to: tabulated material; equations; numerical data; figures and graphics; and references. If you have not already indicated the corresponding author(s) please mark their name(s) with an asterisk. Please e-mail a list of corrections or the PDF with electronic notes attached – do not change the text within the PDF file or send a revised manuscript.

Please bear in mind that minor layout improvements, e.g. in line breaking, table widths and graphic placement, are routinely applied to the final version.

Please note that, in the typefaces we use, an italic vee looks like this: v, and a Greek nu looks like this: ν.

We will publish articles on the web as soon as possible after receiving your corrections; **no late corrections will be made.**

Please return your **final** corrections, where possible within **48 hours** of receipt, by e-mail to: pccp@rsc.org.

Reprints—Electronic (PDF) reprints will be provided free of charge to the corresponding author. Enquiries about purchasing paper reprints should be addressed via: http://www.rsc.org/publishing/journals/guidelines/paperreprints/. Costs for reprints are below:

Reprint costs		
No of pages	Cost (per 50 copies)	
	First	Each additional
2-4	£225	£125
5-8	£350	£240
9-20	£675	£550
21-40	£1250	£975
>40	£1850	£1550
Cost for including cover of journal issue: £55 per 50 copies		

Queries are marked on your proof like this Q1, Q2, etc. and for your convenience line numbers are indicated like this 5, 10, 15, ...

Query reference	Query	Remarks
Q1	[INFO-1] For your information: You can cite this paper before the page numbers are assigned with: (authors), Phys. Chem. Chem. Phys., DOI: 10.1039/c1cp22863c.	
Q2	Please indicate where in the text ref. 4 should be cited.	
Q3	Should the page number for ref. 10 be 3069?	
Q4	Please check the details are correct for ref. 18 and 29	
Q5	Ref. 52: Can this reference be updated yet? Please supply details to allow readers to access the reference.	
Q6	Please provide the full journal name for ref. 64	

PCCP

Dynamic Article Links

Cite this: DOI: 10.1039/c1cp22863c

www.rsc.org/pccp

PAPER

On the interaction of Mg with the (111) and (110) surfaces of ceria

Michael Nolan,*[a] Yaroslava Lykhach,[b] Nataliya Tsud,[c] Tomáš Skála,[d] Thorsten Staudt,[b] Kevin C. Prince,[d] Vladimír Matolín[c] and Jörg Libuda*[be]

Received 8th September 2011, Accepted 16th November 2011
DOI: 10.1039/c1cp22863c

The catalytic activity of cerium dioxide can be modified by deposition of alkaline earth oxide layers or nanoparticles or by substitutional doping of metal cations at the Ce site in ceria. In order to understand the effect of Mg oxide deposition and doping, a combination of experiment and first principles simulations is a powerful tool. In this paper, we examine the interaction of Mg with the ceria (111) surface using both angle resolved X-ray (ARXPS) and resonant (RPES) photoelectron spectroscopy measurements and density functional theory (DFT) corrected for on-site Coulomb interactions (DFT + U). With DFT + U, we also examine the interaction of Mg with the ceria (110) surface. The experiments show that upon deposition of Mg, Ce ions are reduced to Ce^{3+}, while Mg is oxidised. When Mg is incorporated into ceria, no reduced Ce^{3+} ions are found and oxygen vacancies are present. The DFT + U simulations show that each Mg that is introduced leads to formation of two reduced Ce^{3+} ions. When Mg is incorporated at a Ce site in the (111) surface, one oxygen vacancy is formed for each Mg to compensate the different valencies, so that all Ce ions are oxidised. The behaviour of Mg upon interaction with the (110) surface is the same as with the (111) surface. The combined results provide a basis for deeper insights into the catalytic behaviour of ceria-based mixed oxide catalysts.

1. Introduction

Due to its oxygen storage capability, OSC, ceria is widely studied in catalysis.[1–3] A distinguishing feature of ceria is the relative ease with which the oxidation state of Ce changes from oxidised Ce^{4+} to reduced Ce^{3+}, accompanied by formation of oxygen vacancies.[6–17] The reactivity of ceria in oxidation reactions, include CO oxidation[18–20] and NO_X reduction[21–25] is intertwined with the release and uptake of oxygen.

Doping of ceria with other metal cations, such as Zr, La, Pd, Ti and Cu has been widely studied[26–38] to enhance reactivity in oxidation reactions. Also, catalysts based on mixed $MgO–CeO_2$ supports and Mg doping have been proposed for many different reactions.[39–43]

First principles simulations have been applied to study the atomic level properties of undoped[13–17] and doped ceria surfaces,[38,44–48] to rationalise experimental findings and determine the impact of the dopant on the properties of ceria. Dopants include Au,[36,37] Zr,[26] Ti,[38] La,[44] Pt,[45] Pd[46,47] and Ni.[48] These studies have used density functional theory (DFT) corrected for on-site Coulomb interactions (DFT + U),[49,50] and more recently, hybrid DFT with the Heyd-Scuseria-Ernzerhof (HSE)[51,52] functional.

Despite this interest in doped ceria, there have been few studies where experiment and modelling have investigated the electronic structure of doped ceria. In ref. 45, Pt doped ceria (111) was studied with DFT + U in conjunction with experimental characterisation of this catalyst. The modelling was able to provide insights into the experimental findings.

Recently, in the context of CO_2 reduction, which is a route to production of hydrocarbons, we have performed a number of studies examining CO_2 reduction at ceria modified with Mg.[53–55] In these works the interaction of Mg and ceria (111) films grown on Cu was also studied with photoelectron spectroscopy (PES) and resonant PES (RPES), to characterise the nature of the electronic states in the oxide after introduction of Mg.

In this paper, we present comprehensive results of a study using first principles DFT + U and hybrid DFT simulations along with experiments to study the interaction of the ceria (111) and (110) surfaces with Mg. Mg is introduced as (i) an adsorbate and (ii) as a substitutional dopant in both surfaces. The (111) surface is the best characterised ceria surface,[56,57]

[a] *Tyndall National Institute, University College Cork, Lee Maltings, Cork, Ireland. E-mail: michael.nolan@tyndall.ie*
[b] *Lehrstuhl für Physikalische Chemie II, Department Chemie und Pharmazie, Friedrich-Alexander-Universität Erlangen-Nürnberg, Egerlandstr. 3, 91058 Erlangen, Germany. E-mail: joerg.libuda@erlangen.de*
[c] *Charles University in Prague, Faculty of Mathematics and Physics, Department of Surface and Plasma Science, V Holešovičkách 2, 18000 Prague 8, Czech Republic*
[d] *Sincrotrone Trieste SCpA, Strada Statale 14, km 163.5, 34149 Basovizza-Trieste, Italy*
[e] *Erlangen Catalysis Resource Center, Friedrich-Alexander-Universität Erlangen-Nürnberg, Egerlandstr. 3, 91058 Erlangen, Germany*

while the (110) surface tends to be the more reactive surface.[58,59]

The experimental results show that when Mg is deposited at the (111) surface, reduced Ce^{3+} ions and Mg^{2+} are formed; this result is also found in the DFT calculations at the (111) and (110) ceria surfaces. In the latter, two surface Ce ions are reduced to Ce^{3+}. Further annealing and oxidation indicates incorporation of Mg into the CeO_{2-x} matrix and the presence of only Ce^{4+}. From the calculations, doping Mg onto a Ce site leads to spontaneous formation of oxygen vacancies, without formation of Ce^{3+}. In addition, a notable reduction in the formation energy of catalytically active oxygen vacancies is found. Thus, a combined experiment and DFT modelling investigation can provide deep insights into catalytically important model systems.

2. Methodology

Experimental

Angle resolved X-ray (ARXPS) and resonant (RPES) photoelectron spectroscopy measurements were performed at the Materials Science Beamline, Elettra (Trieste, Italy). Photoelectron spectra were acquired with a high luminosity electron energy analyzer (Specs Phoibos 150), equipped with a 9 channel detector. For the ARXPS we used a dual Al/Mg X-ray source. Core level spectra of Ce 3d, Cu $2p_{3/2}$, O 1s, Mg 1s and C 1s were acquired using Al–Kα (1486.6 eV) radiation. The SRPES measurements employed a bending magnet synchrotron source that produced linearly polarized light in the energy range of 21–1000 eV. The resonant photoelectron spectra of the valence band were recorded at photon energies (PEs) $h\nu$ = 115, 121.4 and 124.8 eV. All spectra were taken at constant pass energy, at emission angles of the photoelectrons (γ) of 20° and 60° for the Al Kα and of 0° for the synchrotron radiation with respect to the sample normal. The spectra measured with the synchrotron light were normalized with respect to the ring current and acquisition time. The total spectral resolution achieved with the Al Kα and synchrotron radiation was 1 eV and 150–200 m eV, respectively. Ce 3d, O 1s, C 1s, and Mg 1s core level spectra were fitted with Voigt profiles after subtraction of Shirley background.

The experimental end station was equipped with a rear-view LEED optics, a quadrupole mass spectrometer, an ion gun, and a gas inlet system. The background pressure in the analysis chamber was better than 2×10^{-10} mbar during all measurements.

A single crystal Cu(111) disc (MaTecK) was cleaned by several cycles of Ar^+ ion sputtering (at 300 K for 60 min) and annealing (723 K for 5 min) until no traces of carbon or other contaminants were found in the photoelectron spectra. Epitaxial layers of CeO_2(111) were grown on clean Cu(111) by physical vapor deposition (PVD) of Ce metal (Goodfellow, 99.99%) at an oxygen partial pressure of 5×10^{-7} mbar (Linde, 99.995%) at 523 K, followed by annealing of the films at 523 K in an oxygen atmosphere of the same pressure for 10 min. LEED measurements revealed a well-ordered CeO_2(111) film with a (1.5 × 1.5) superstructure with respect to Cu(111). The prepared films typically reveal flat terraces separated by steps, with the top terraces often covered with small ceria aggregates. The thickness of the prepared films was determined from the attenuation of the Cu $2p_{3/2}$ signal, acquired using Al–Kα X-ray source at $\gamma = 20°$. A value of 1.5 nm was measured, corresponding to about 5 monolayers (MLs) of ceria. Here we define 1 ML as one O–Ce–O trilayer of CeO_2(111), corresponding to thickness of 0.313 nm.[5] For further details concerning the preparation procedure we refer to the literature.[54,56,57,60] Mg metal (Goodfellow, 99.9%) was deposited from a resistively heated Mo crucible onto the fully stoichiometric CeO_2 film at 300 K. The amount of the deposited material was estimated by the attenuation of the intensity of the Cu $2p_{3/2}$ photoemission signal, acquired using an Al–Kα X-ray source at $\gamma = 20°$. The estimated thickness of Mg was about 0.6 nm. The deposition was followed by annealing to 700 K. Finally, the samples were exposed to an oxygen atmosphere (5×10^{-7} mbar, 1000 s) at 523 K and subsequently annealed to 700 K.

Annealing was done using a DC power supply passing a current through Ta wires that held the sample. The temperature was measured by a K-type thermocouple attached to the rear surface of the sample.

DFT + U and hybrid DFT simulations

In describing ceria (111) and (110) surfaces, a three dimensional periodic slab model and a plane wave basis set description of the valence electronic wave functions are used within the VASP code.[61] The cut-off for the kinetic energy is 400 eV. Blöchl's projector augmented wave (PAW) approach[62] describes the core-valence interactions; Ce has a 12 valence electron potential, Mg has two valence electrons and O has a [He] core.

We use the Perdew-Wang91 approximation to the exchange–correlation functional.[63] k-point sampling is performed using the Monkhorst–Pack scheme, with (2 × 2 × 1) and Γ-point sampling grids, depending on the surface supercell expansion.

In the Tasker classification, the (111) surface is type II[64] and is made up of neutral O–Ce–O tri-layers along the slab with no dipole after cleaving. The (110) surface is type I, with neutral CeO_2 planes in each surface layer. For the (111) surface (2 × 2) and (4 × 4) surface supercell expansions were employed (as discussed in ref. 65), while for the (110) surface, a (2 × 4) and (2 × 2) surface expansions have been tested. For the (111) surface, the slab is 4 O–Ce–O trilayers thick (12 atomic layers, 6% and 1.5% Mg dopant/adsorbate concentrations), while the (110) surface slab is 7 layers thick, giving 56 Ce ions in the larger surface supercell, with 8 Ce ions in the surface layer, giving an overall dopant concentration of 1.8%. The vacuum gap is 12 Å.

The process of oxide reduction, so important in ceria, is described through formation of an oxygen vacancy requiring that oxidised and reduced Ce are treated consistently. To describe oxide reduction in CeO_2 requires an approach such as DFT + U[66] or hybrid DFT.[46,47] The application of DFT + U to ceria is well known and will not be discussed here.[10–17,20–22,39–44] In our work, the U parameter is 5 eV on Ce 4 f states.[12,13]

Hybrid DFT adds a portion of exact Hartree–Fock exchange to the local DFT energy, which helps to partially correct the self-interaction problem with local DFT. 25% exact exchange is applied and this is a universal parameter. The screened exchange functional of Heyd-Scuseria-Ernzerhof (HSE) is used,[46,47] with a universal screening parameter of 0.2/Å. Due to the large computational expense of hybrid DFT calculations in a plane wave basis set, we limit hybrid DFT to the (2 × 2) surface supercell expansion of the (111) surface, providing a check on the performance of DFT + U; applications of hybrid DFT to ceria can be found in recent papers.[17,52,67,68]

3. Results

3.1 Experimental results on the interaction of Mg with CeO_2(111): ARXPS and RPES

We have studied the interaction of Mg with the CeO_2(111) surface using a CeO_2(111) thin film grown on Cu(111) (see Fig. 1 and 2(a)). The film is composed of about five O–Ce–O trilayers. Two monolayer equivalents of Mg were deposited at 300 K (see Fig. 1 and 2b). Subsequently, we consider the behaviour of the film upon annealing to 700 K (see Fig. 1 and 2c) and reoxidation by O_2 (at 523 K with subsequent annealing to 700 K, see Fig. 1 and 2d).

The core levels of Ce 3d, O 1s, and Mg 1s obtained using Al Kα radiation at $\gamma = 60^\circ$ before and after Mg deposition are shown in Fig. 1a and b, respectively. The characteristic Ce 3d spectrum of stoichiometric CeO_2(111) is composed of three spin- orbit doublets (ν–u, ν″–u″, and ν‴–u‴) due to the three photoemission final states evolving upon 3d core ionization of Ce^{4+} (see ref. 1 for more details). The corresponding O 1s spectrum has a single component at a BE of 529.4 eV.

A related set of the valence band spectra (resonant photoelectron spectra) from the CeO_2(111) film obtained at PEs of 115, 121.4, and 124.8 eV is shown in Fig. 2a. The valence band spectra measured at PEs of 124.8 and 121.4 eV show a resonant enhancement of photoemission features related to Ce^{4+} and Ce^{3+} ions, respectively. The spectrum at a PE of 115 eV corresponds to the off-resonance condition.[69] The principal features of the spectra, which are associated with O 2p hybridization with Ce 4f and 5d orbitals, have been discussed previously, *e.g.* by Mullins *et al.*[70] Resonantly enhanced features related to Ce^{4+} appear in the VB at binding energies (BE) of 4 eV, Ce^{3+} related features at 1.5–2 eV. The individual resonant enhancements for Ce^{4+} (denoted as D(Ce^{4+})) and Ce^{3+} (denoted as D(Ce^{3+})) are determined from the intensity differences between the corresponding features in- and off-resonance position (see *e.g.* ref. 69). They reflect the variations of the oxidation state of cerium as a function of the preparation conditions, with enhanced sensitivity with respect to the Al K_α-excited Ce 3d core levels.[69]

We now consider the spectra for the freshly prepared CeO_2(111) film before Mg deposition (Fig. 2a). For in-resonance conditions we observe a significant increase of the intensity at around 4 eV (D(Ce^{4+})) and only a very weak enhancement at 1.5 eV (D(Ce^{4+})). This reflects the nearly perfect stoichiometry of the CeO_2(111) film which contains a very small concentration of oxygen vacancies only.

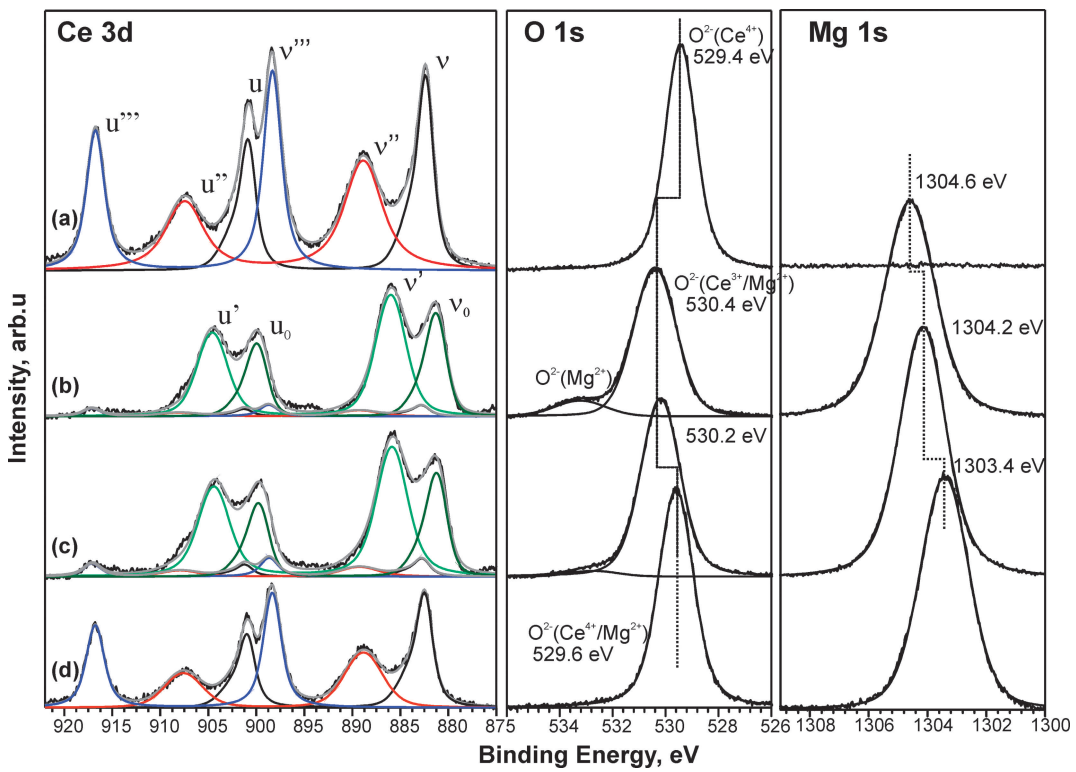

Fig. 1 Ce 3d, O 1s, and Mg 1s core level spectra obtained using Al Kα radiation at $\gamma = 60^\circ$ from stoichiometric CeO_2(111)/Cu(111) film (a) after deposition of Mg at 300 K (b), followed by annealing to 700 K (c), followed by oxidation at 523 K with subsequent annealing to 700 K (d).

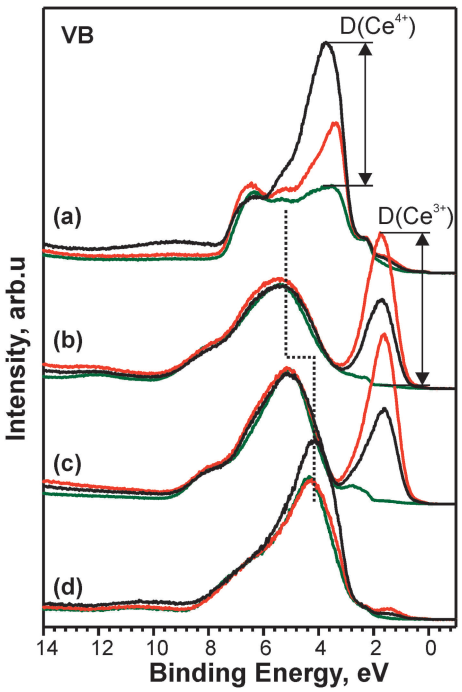

Fig. 2 Sets of valence band photoelectron spectra obtained with photon energies corresponding to resonant enhancements in Ce^{4+} (124.8 eV, black) and Ce^{3+} (121.4 eV, red), and to off-resonance (115 eV, green) from the stoichiometric CeO_2(111)/Cu(111) film (a) after deposition of Mg at 300 K (b), followed by annealing to 700 K (c), followed by oxidation at 523 K with subsequent annealing to 700 K (d). The resonant enhancements in Ce^{4+} and Ce^{3+} give rise to D(Ce^{4+}) and D(Ce^{3+}) features at 4.1 and 1.5–2 eV, respectively.

Deposition of Mg onto the stoichiometric CeO_2(111) at 300 K causes immediate reduction of ceria and oxidation of Mg. Facile conversion of Ce^{4+} into Ce^{3+} is evident from the analysis of the Ce 3d spectrum displayed in Fig. 1b. The two doublets ($\nu_o - u_o$ and $\nu' - u'$)[69] which emerge are characteristic for Ce^{3+}. Only a very small contribution from the Ce^{4+} remains in the spectra (see fit displayed in Fig. 1b). The efficient reduction is consistent with appearance of a strong D(Ce^{3+}) resonant enhancement feature appearing in the valence band spectrum shown in Fig. 2b. The corresponding O 1s spectrum shows a shift of the major component from 529.4 eV to 530.4 eV which is accompanied by the emergence of a weak shoulder at 533.2 eV. The relative intensity of the shoulder is dependent on the detection angle. The higher intensity at $\gamma = 60^\circ$ suggests that its origin is related to a surface species, such as a surface defect site. Similar BEs were reported, for example, for MgO (530.4–531.0 eV)[71] and defect rich surfaces such as *e.g.* $Mg(OH)_2$ (533.2 eV),[71] respectively. In the Mg 1s region a single peak is observed at 1304.6 eV. A comparison with typical BE ranges reported for Mg 1s (Mg^0: 1303.1–1303.2 eV; MgO: 1304.1–1305.0 eV; $Mg(OH)_2$: 1305.0 eV)[72] suggests that Mg is quantitatively oxidized to Mg^{2+} upon deposition at 300 K.

From the above discussion, we conclude that Mg deposition leads to formation of a defect-rich containing MgO-like layer and facile reduction of Ce^{4+} to Ce^{3+}. It is worth noticing that according to the bulk phase diagram, MgO and CeO_2 are nearly immiscible and do not form any ternary compounds.[72] However, formation of non-equilibrium MgO–CeO_2 solid mixtures was reported by several authors.[73,74]

In order to obtain a rough estimate of the possible composition of the MgO–CeO_{2-x} deposit, some XPS simulations were performed using SESSA V1.1.[75] A schematic representation of Mg–CeO_2 structures considered in the XPS simulations is shown in Fig. 3. We tested various distribution profiles of deposited MgO layers within the CeO_{2-x} film. A comparison of the experimental and simulated ratios of the core level intensities (Ce 3d and Mg 1s) at two emission angles (γ) is given in Table 1 for three selected model structures: (I) A model structure assuming no intermixing, *i.e.* a pure MgO film (0.6 nm) on top of five O–Ce–O trilayers; (II) a model assuming complete intermixing (six O–(0.2 Mg; 0.8 Ce)–O trilayers); and (III) a model assuming partial intermixing (three oxygen deficient trilayers O–($a \times$ Mg; $b \times$ Ce)–O; 1st layer: (1.00 Mg; 0.00 Ce), 2nd layer: (0.67 Mg; 0.33 Ce), 3rd layer: (0.33 Mg; 0.67 Ce) on top of four O–Ce–O trilayers).

The comparison of the simulated and experimental data (see Table 1) shows that neither a pure MgO overlayer nor the complete intermixing model can account for the experimental intensity ratios. The depth profile of the MgO–CeO_{2-x} film is best described by model (III) assuming partial intermixing. Any further modifications of the Mg–CeO_2(III) profile did not return any better match of the calculated and the experimental values. The simulations suggest that intermixing of Mg^{2+} and Ce^{3+} at 300 K occurs within few (approximately two) layers at the interface with the topmost layer dominated by MgO. Furthermore, the model is compatible with the presence of oxygen deficiencies in the Mg-containing layers on top of pure O–Ce–O layers with Ce_2O_3 stoichiometry.

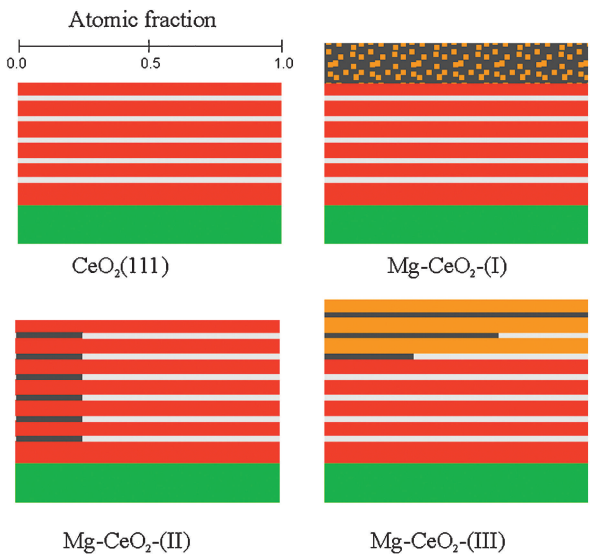

Fig. 3 Schematic representation of CeO_2(111), Mg–CeO_2 – (I), Mg–CeO_2 – (II), and Mg–CeO_2 – (III) compositions considered in XPS simulations. Different colours represent layers of cerium (light grey), oxygen (red), oxygen deficient (yellow), magnesium (dark gray), and a film of amorphous magnesia (dark gray and yellow patterns). The Cu(111) substrate is shown in green.

Table 1 The experimental (exp.) and simulated (sim.) intensity ratios of Ce 3d and Mg 1s core levels measured at $\gamma = 60^\circ$ and $\gamma = 20^\circ$. The entries in bold indicate the experimental intensity ratio and the model that best agrees with experiment

	I^{60}_{Ce}/I^{20}_{Ce}		I^{60}_{Mg}/I^{20}_{Mg}	
Sample structure	Exp.	Sim.	Exp.	Sim.
CeO_2(111)	1.040	1.003	—	—
Mg–CeO_2 – (I)	**0.769**	0.727	**0.789**	1.100
Mg–CeO_2 – (II)		1.180		0.994
Mg–CeO_2 – (III)		**0.788**		**0.789**

Finally, we briefly consider the changes of the MgO–CeO_{2-x} film upon annealing and reoxidation. Upon annealing to 700 K, the spectral shape in the Ce 3d spectrum is not affected. However, a slight change in the intensity ratios $I^{60}_{Ce}/I^{60}_{Mg}(I^{20}_{Ce}/I^{20}_{Mg})$ of Ce to Mg at $\gamma = 60^\circ$ ($\gamma = 20^\circ$) is observed from 1.56 (1.60) to 1.75 (1.70) after annealing. This change indicates a slight increase of Ce^{3+} concentration at the surface. The corresponding O 1s and Mg 1s peaks shift to lower BE by 0.2 and 0.4 eV, respectively. A similar BE shift (0.3 eV) is observed for the major valence band feature at a BE of 5.0 eV. The rigid shift suggests that the effect is mainly due to a change of the electrostatic potential related to diffusion of Mg ions into deeper ceria layers.

Finally, the preannealed Mg deposit on CeO_2 is exposed to an oxygen atmosphere at 523 K, followed by annealing at 700 K. After this treatment, only features related to Ce^{4+} ($\nu - u$, $\nu'' - u''$, and $\nu''' - u'''$ components) are observed in the Ce 3d spectrum. In accord with this, we observe that in the RPE spectra the D(Ce^{3+}) resonant feature diminishes, whereas a strong D(Ce^{4+}) feature appears (see Fig. 2d). We conclude that oxygen treatment leads to complete conversion of Ce^{3+} ions to Ce^{4+}. After reoxidation, the O 1s signal shifts to 529.6 eV, a BE value similar to that of stoichiometric CeO_2. Surprisingly, the Mg 1s peak also shifts to lower BE by −0.8 eV. The resulting value of 1303.4 eV is clearly below those typically observed for MgO.[68] We attribute this change to a change in the chemical surrounding of the Mg^{2+} ions, suggesting that Mg^{2+} is incorporated into the ceria matrix.

3.2 Modelling the interaction of Mg with the (111) and (110) surfaces of CeO_2

In Fig. 4 we show the atomic structure of the bare CeO_2(111) and (110) surfaces.[45,46] The (111) surface has 7 coordinate surface Ce and 3 coordinate surface oxygen, with Ce–O distances slightly shortened over the bulk oxide, at 2.36 Å. In the surface layer, the (110) surface has 6 coordinate Ce and surface oxygen are 3 coordinate, with surface Ce–O distances of 2.32 Å.

The (111) surface is the most stable, as determined from surface energies and is the most commonly exposed surface in experimental samples. The (110) surface has the lowest computed oxygen vacancy formation energy,[46] making it the most reactive.

We first consider adsorption of Mg at the (111) and (110) ceria surfaces. Fig. 5 shows the most stable adsorption structure of Mg at the (111) and (110) ceria surfaces, determined from DFT + U. On the (111) surface, we observe that Mg

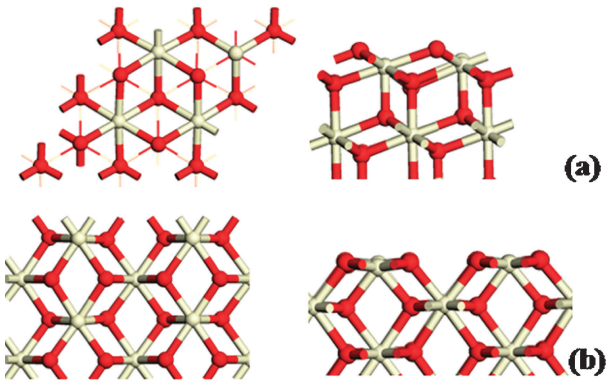

Fig. 4 Atomic structure of the bare CeO_2 surfaces. (a) (111) and (b) (110). In this and subsequent figures, Ce is coloured white and O is red.

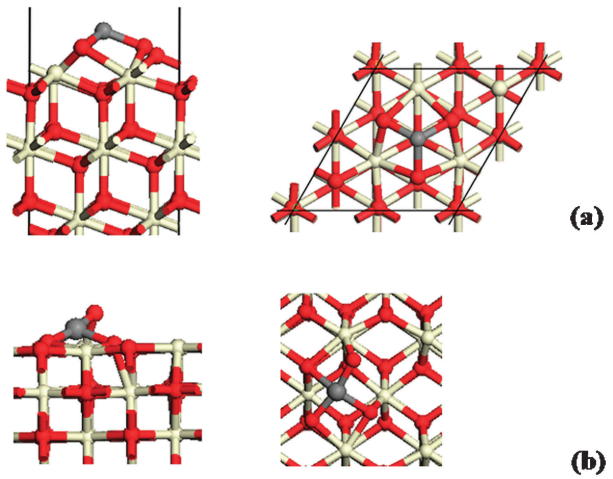

Fig. 5 Atomic structure of Mg adsorbed at the (a) (111) and (b) (110) surfaces of ceria. In the interest of space, only a portion of the (110) surface around the dopant site is shown. The dopant is the grey sphere.

binds to three surface oxygen atoms. These oxygen atoms are displaced by 0.46 Å off their initial lattice sites to form Mg–O bonds, with Mg–O distances of 1.95 Å and Ce–O distances in the range of 2.35–2.56 Å. In the interaction of Mg with surface oxygen, these oxygen are also displaced in the surface plane (apparent from the plan view in Fig. 5a), while a symmetric structure around the Mg adsorption site is retained, but distorted from the original hexagonal symmetry in the bare surface. We have checked that there are no distorted structures lower in energy than the adsorption structure shown in Fig. 5.

Upon adsorption at the (110) surface, Mg interacts with four surface oxygen atoms, and displaces three of them off their initial lattice sites to form a 4 coordinate Mg species. One oxygen atom is displaced by 1.55 Å from its initial surface lattice site, with a bond length of 1.92 Å to Mg. Two further oxygen atoms are displaced by 0.24 Å and 0.15 Å, giving bond lengths of 2.10 Å and 2.01 Å to Mg. The last oxygen is undisturbed and has a bond length of 2.14 Å to Mg. The displacement of oxygen from the surface lattice sites perturbs the local atomic structure around the adsorption site, with the most displaced oxygens showing Ce–O distances up to 3.42 Å

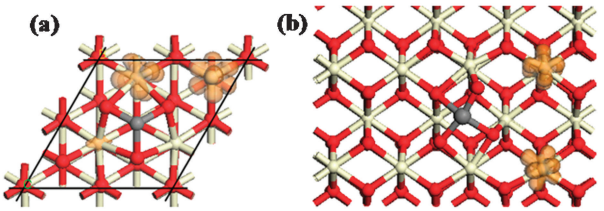

Fig. 6 Spin density plot for Mg adsorbed at the (a) (111) and (b) (110) surfaces of ceria. The spin density isosurfaces are orange and include spin densities up to 0.02 electrons/Å^3.

and 4.2 Å long, but with stronger binding to other surface Ce, with Ce–O distances of 2.27 Å and 2.04 Å.

Fig. 6 shows the excess spin density for Mg adsorbed at both surfaces, which is used to characterise the location of any reduced Ce cations. At both surfaces, Mg adsorption leads to oxidation of Mg to Mg^{2+}, and formation of two reduced Ce^{3+} species, as indicated by the two Ce ions with the non-zero spin density isosurfaces in Fig. 6, which can be written in Kroger-Vink notation as $Mg^{\bullet\bullet}_{ads}2Ce'_{Ce}$. The two Ce^{3+} ions are found in the outermost Ce layer of each surface. This is consistent with the results of Fig. 1b and 2b, for which the change of the oxidation state of cerium from Ce^{4+} to Ce^{3+} is evident upon deposition of Mg at the (111) surface.

The experimental results suggest possible incorporation of Mg in an "interstitial" site in the (111) surface, which is denoted as $Mg_i^{\bullet\bullet}2Ce'_{Ce}$ and we have performed some DFT + U calculations of Mg in interstitial sites of the (111) surface. Fig. 7 shows the position of Mg in the two interstitial subsurface sites in the (111) surface. The structure in Fig. 6b is the more stable and the spin density is shown in Fig. 6c.

In the most stable Mg interstitial site, it is interesting to observe that during the relaxation, Mg moves towards a lattice Ce site, that is a site in the first layer of surface Ce ions. At the same time, this Ce atom is displaced off its lattice site, away from the surface and is found lying in the same plane as the outermost oxygen atoms of the surface. Thus, Mg displaces a Ce ion from the outermost layer of Ce atoms in the (111) surface and this structure is 0.4 eV more stable than the structure shown in Fig. 7a. In the most stable structure, Mg is oxidised, with reduction of two neighbouring Ce sites to Ce^{3+}.

We now consider substitutional Mg doping of the ceria (111) and (110) surfaces, which can be written as $Mg_i^{\bullet\bullet}2Ce'_{Ce}$; the experimental data indicate incorporation of Mg in the matrix of the CeO_2(111) surface, with only Ce^{4+} present with an accompanying oxygen deficiency. In the doping, Mg is preferentially found in the outermost layer of Ce ions in each surface. For the (111), surface we present results on the (2 × 2) surface supercell with DFT + U and HSE06, providing a useful check on the DFT + U results.

In the (111) surface, the 7-fold Ce coordination environment is not favourable for the dopant (see also ref. 43) and Mg distorts the local structure to obtain an environment that is more favourable, which involves four-fold coordination to one surface oxygen, two subsurface oxygen and a fourth (atomic) layer oxygen. This involves displacement of Mg away from the remaining three surface oxygen atoms. This distortion is again evident from both DFT approaches. The distortion around

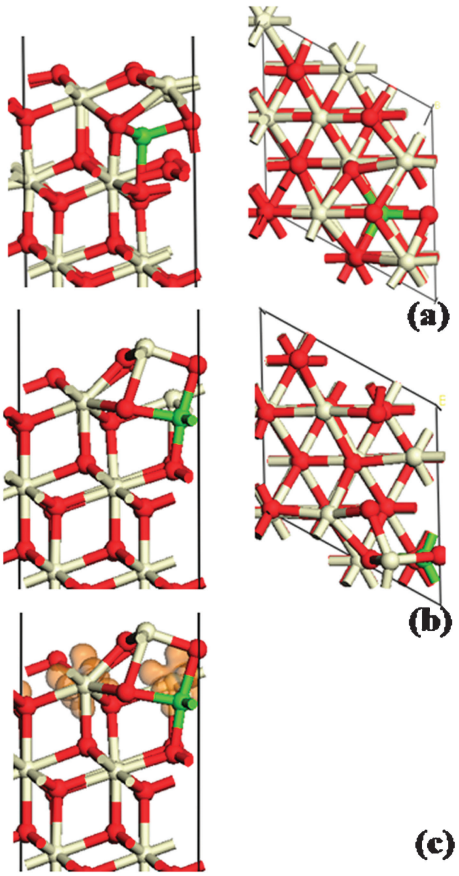

Fig. 7 The relaxed CeO_2(111) surface with Mg incorporated in subsurface interstitial sites. (a) site I, (b) site II and (c) spin density of Mg incorporation in site II. The spin density isosurfaces are orange and include spin densities up to 0.02 electrons/Å^3.

the dopant occurs quite naturally, with no symmetric, undistorted solution found.

In Fig. 8a and b we show the structure of Mg substituted into the (111) surface from DFT + U and hybrid DFT, respectively. Fig. 8c shows the atomic structure of Mg in the (110) surface of CeO_2; the most stable substitutional site is in the surface layer, where a 6-fold coordinated Ce ion is substituted with the dopant.

Table 2 shows the Mg–O distances in the doped surfaces. We see that the Mg–O distances are notably shorter than the Ce–O distances, which leads to local distortions to the surface structure. On comparing the geometry data in Table 2 for the two DFT approaches, similar structures are found after doping, which is an encouraging result.

In the (110) surface, there are also localised distortions around the Mg lattice site—Mg–O distances, while longer than those in rock salt Mg–O are notably shorter compared with the Ce–O distances. In particular, the dopant sinks into the bulk to have rather short Mg–O distances to the oxygen in the first subsurface layer. The geometry of the surface oxygen atoms, while distorted by their motion towards Mg, remains quite symmetric upon doping.

Since Mg has a +2 oxidation state, giving the defect $Mg^{\bullet\bullet}_{Ce}2O^{\bullet}_{O}$, with the well-known oxygen hole polaron found when a lower valent dopant substituted a higher valent cation,

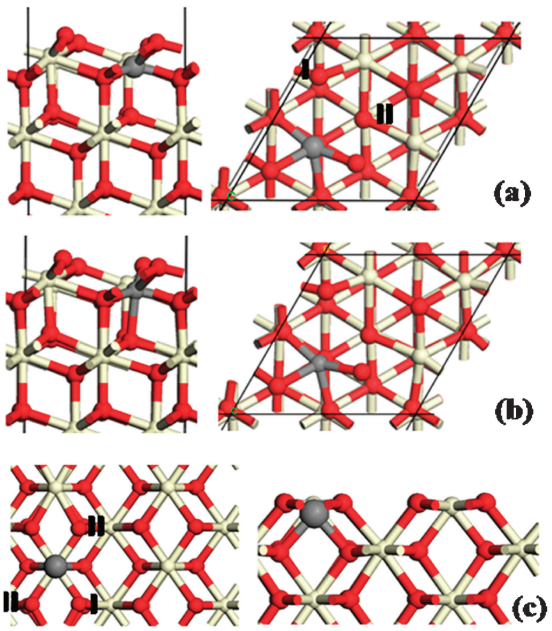

Fig. 8 The relaxed CeO_2(111) and (110) surfaces doped with Mg. (a) DFT + U (111) (2 × 2) surface supercell, (b) hybrid DFT (111) (2 × 2) surface supercell, (c) DFT + U (110) (2 × 2) surface supercell. The compensating oxygen vacancy sites are indicated in (a) and (c) for comparison with Table 3. The black lines show the edge of the supercell.

Table 2 Mg–O distances in Mg doped (111) (2 × 2) surface supercell with DFT + U and HSE and the (110) (2 × 2) surface supercell with DFT + U

Method	M–O surface layer	M–O first subsurface layer	M–O fourth layer
(111) Surface			
DFT + U	2.09, 2.24	2.07, 2.08	2.15
HSE	2.11, 2.22	2.04, 2.05	2.13
(110) Surface			
DFT + U	2.21, 2.21 2.24, 2.25	2.08, 2.09	

the lower valence of Mg can be compensated by formation of an oxygen vacancy, without formation of Ce^{3+} species. We compute the energy of oxygen vacancy formation in the doped surfaces from

$$E(O_{vac}) = \{E(1/2O_2) + E(MgCeO_{2-x})\} - E(MgCeO_2), \quad (1)$$

where $E(MgCeO_{2-x})$ is the total energy of the Mg doped CeO_2 surface and an oxygen vacancy, $E(MgCeO_2)$ is the total energy of the Mg-doped CeO_2 surface and we reference to half the energy of an O_2 molecule. This defect is written: $Mg''_{Ce}Ce^{x}_{Ce}O^{x}_{O}$, *i.e.* with all Ce ions with a Ce^{4+} oxidation state. If the oxygen vacancy formation energy is negative then an oxygen vacancy will form spontaneously to compensate the dopant. Fig. 8 shows the sites considered for oxygen vacancy formation in both surfaces, with the dopant indicated as the grey sphere and the oxygen vacancy sites we have considered are numbered I and II in the (111) surface, Fig. 8a. Fig. 8c shows the dopant and vacancy sites, numbered I–III, for the (110) surface.

In both ceria surfaces, the energy of oxygen vacancy formation shows that doping with divalent Mg is spontaneously compensated by formation of an oxygen vacancy, indicated by the negative oxygen vacancy formation energies in Table 3. In addition, all Ce ions have a Ce^{4+} oxidation state. The presence of only Ce^{4+} agrees with the results in Fig. 1(d) and 2(d) in which Mg is incorporated with only Ce^{4+} present.

Considering briefly the energetics of oxygen vacancy formation to compare DFT + U and HSE06, while both DFT methods give different absolute energies for the oxygen vacancy formation energy, with HSE06 more strongly favouring vacancy formation, the important finding is that both approaches give spontaneous formation of the oxygen vacancy to compensate the dopant in both surfaces so that DFT + U can be used to study the properties of these systems. Further discussions in this vein can be found in ref. 65.

Fig. 9a and b shows the most stable oxygen vacancy compensation structure the Mg doped (111) surface from DFT + U and HSE06, while Fig. 9c shows the most stable oxygen vacancy compensation structure in the Mg doped (110) surface. Mg being much smaller than Ce, when comparing ionic radii, strongly distorts the structure around itself. In the (111) surface, Mg now coordinates to two subsurface oxygen atoms, with Mg–O distances to subsurface oxygen of 2.03 and 2.06 Å and to a fourth layer oxygen, with an Mg–O distance of 2.10 Å, with the dopant noticeably sinking into the surface.

In the (110) surface, Mg strongly distorts the local atomic structure, showing two short Mg–O distances to two subsurface oxygen ions, with Mg–O distances of 2.01, 2.07 Å Mg also coordinates to two surface oxygens, with a distance of 2.16 Å and the remaining surface Mg–O distance is elongated to 2.28 Å.

The final part of this study concerns the energetics of formation of an active oxygen vacancy in Mg doped ceria surfaces. This is the oxygen that would be active in, *e.g.* CO oxidation *via* the Mars van Krevelen mechanism. A number of oxygen sites in both doped, vacancy compensated surfaces are indicated in Fig. 10a and b for both doped surfaces and these oxygen are removed and the formation energy of the oxygen vacancy is computed:

$$E(2O_{vac}) = \{E(MgCeO_{2-y}) + E(1/2O_2)\} - E(MgCeO_{2-x})\}, \quad (2)$$

where $E(MgCeO_{2-v})$ is the total energy of the Mg-doped CeO_2 surface with two oxygen vacancies, $E(MgCeO_{2-x})$ is the total energy of the Mg-doped CeO_2 surface with the compensating oxygen vacancy and we reference to half the energy of an O_2 molecule. These calculations are carried out with DFT + U, since the previous results indicate the reliability of DFT + U in the present systems. Table 4 gives the formation energy for

Table 3 Formation energies (eV) of compensating oxygen vacancies in Mg doped CeO_2 surfaces. The most stable vacancy sites are highlighted in bold font

Surface	(111) DFT + U	(111) HSE06	(110)
O vacancy I	−0.22	−0.95	**−0.70**
O vacancy II	**−1.07**	**−1.80**	**−0.70**
O vacancy III	—	—	**−0.70**

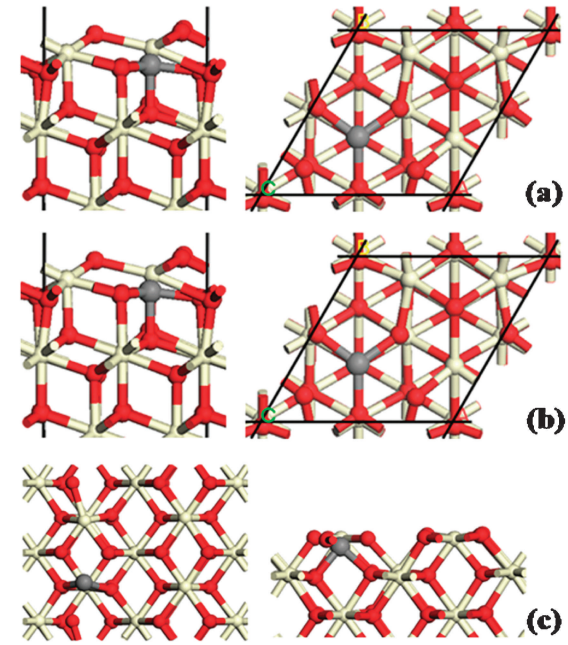

Fig. 9 The most stable oxygen vacancy compensated structures for Mg doping. (a) (111) surface DFT + U, (b) (111) surface HSE06 (c) (110) surface DFT + U.

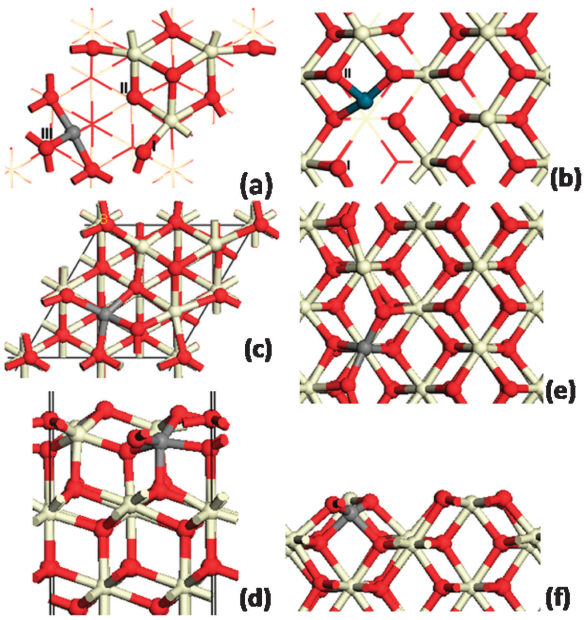

Fig. 10 Oxygen vacancy sites considered for formation of an active oxygen vacancy in Mg doped CeO_2 surfaces; (a): (111) and (b): (110). (c) and (d) show the relaxed structures of the most stable active oxygen vacancy site in the (111) surface and (e) and (f) show the relaxed structure of the most stable active oxygen vacancy site in the (110) surface.

the active oxygen vacancy and Fig. 10c–f shows the relaxed atomic structures.

In the Mg doped (111) surface, removal of any oxygen considered is more favourable than in the undoped surface, as indicated by the computed formation energies (in the undoped surface the cost of forming an oxygen vacancy is 2.66 eV[10]). This arises since Mg is able to coordinate to four oxygen atoms in each case and appears to have no obviously preferred coordination environment—the differences in the computed formation energies are no more than 0.2 eV. Upon formation of the active oxygen vacancy, Mg remains coordinated to four oxygen ions, but there is a change in the exact coordination environment as the dopant seeks to maintain bonding to four oxygen atoms.

Table 4 Formation energies in eV of active oxygen vacancies in Mg doped CeO_2(111) and (110) surfaces from DFT + U

Surface	(111)	(110)
O vacancy I	1.65	2.43
O vacancy II	1.47	1.85
O vacancy III	1.25	—

In the (110) surface, the energetics show that there is a preference for the position of the active oxygen vacancy in the surface, with position II in Fig. 10 being the more favourable. This is due to Mg retaining its preferred coordination environment in the second oxygen vacancy structure, compared to the first oxygen vacancy structure. The second oxygen vacancy structure involves removing the surface oxygen with the longest Mg–O distance, which is obviously more favourable.

In both Mg-doped CeO_2 surfaces, the formation of the active oxygen vacancy leads to reduction of two Ce^{4+} ions to Ce^{3+}, giving the defect, $Mg_{Ce}^{\bullet\bullet}2Ce'_{Ce}$, typical of Ce reduction in neutral CeO_2.

4. Conclusions

In comparing the experimental and DFT results for the interaction of Mg with the ceria (111) and (110) surfaces, we can summarise the key findings from our study:

(1) Deposition of Mg at the (111) surface leads to oxidation of Mg to Mg^{2+} and formation of reduced Ce^{3+} species. The DFT calculations give the same result.

(2) Incorporation of Mg into the (111) surface in subsurface interstitial sites also results in formation of reduced Ce^{3+} species and Mg oxidation.

(3) Such Mg-doped ceria layers can experimentally be prepared by Mg deposition onto stoichiometric CeO_2 films, post-oxidation and annealing.

(4) Substitution of Mg onto a Ce site is accompanied by removal of oxygen, but without formation of Ce^{3+} sites. This results from charge compensation of the lower valence Mg^{2+} dopant by formation of oxygen vacancies, which, from the calculations, is spontaneous.

(5) Formation of catalytically active oxygen vacancies is more favourable in the Mg doped surface compared with the undoped surface.

(6) At the (110) surface, the calculations indicate that Mg shows the same behaviour.

These results show that the combination of model catalyst synthesis, RPES and high level DFT simulations is a powerful approach to understand catalytically active materials systems.

Acknowledgements

MN acknowledges support from Science Foundation Ireland through the Starting Investigator Research Grant Program, project "EMOIN" grant number SFI 09/SIRG/I1620. We also acknowledge computing resources provided by SFI to the Tyndall National Institute and by the SFI and Higher Education Authority Funded Irish Centre for High End Computing.

The authors acknowledge financial support by the Deutsche Forschungsgemeinschaft (DFG). Additional support by the DFG was provided within the Excellence Cluster "Engineering of Advanced Materials" in the framework of the excellence initiative. We acknowledge support by the Fonds der Chemischen Industrie, the DAAD, and Ministry of Education of the Czech Republic (LA08022) and of the Czech Grant Agency (P204/10/1169).

References

1 A. Trovarelli, *Catalysis by Ceria and Related Materials*, Imperial College, UK, 2002.
2 A. Trovarelli, *Catal. Rev. Sci. Eng.*, 1996, **38**, 439.
3 R. J. Gorte, *AIChE J.*, 2010, **56**, 1126.
4 L. Vivier and D. Duprez, *ChemSusChem*, 2010, **3**, 654.
5 M. A. Henderson, C. L. Perkins, M. H. Engelhard, S. Thevuthasan and C. H. F. Penden, *Surf. Sci.*, 2003, **526**, 1.
6 L. Chen, P. Fleming, V. Morris, J. D. Holmes and M. A. Morris, *J. Phys. Chem. C*, 2010, **114**, 12909.
7 F. Esch, S. Fabris, L. Zhou, T. Montini, C. Africh, P. Fornaserio, G. Comelli and R. Rosei, *Science*, 2005, **309**, 752.
8 F. Vasiliu, V. Parvulescu and C. Sarbu, *J. Mater. Sci.*, 1994, **29**, 2095.
9 Y. M. Chiang, E. B. Lavik and D. A. Blom, *Nanostruct. Mater.*, 1997, **9**, 633.
10 M. Nolan, J. E. Fearon and G. W. Watson, *Solid State Ionics*, 2006, **177**, 306.
11 P. R. L. Keating, D. O. Scanlon and G. W. Watson, *J. Phys.: Condens. Matter*, 2009, **21**, 405502.
12 S. Fabris, S. de Gironcoli, S. Baroni, G. Vicario and G. Balducci, *Phys. Rev. B: Condens. Matter Mater. Phys.*, 2005, **71**, 041102.
13 M. Nolan, S. Grigoleit, D. C. Sayle, S. C. Parker and G. W. Watson, *Surf. Sci.*, 2005, **576**, 217.
14 M. Nolan, S. C. Parker and G. W. Watson, *Surf. Sci.*, 2005, **595**, 223.
15 S. Fabris, G. Vicario, G. Balducci, S. de Gironcoli and S. Baroni, *J. Phys. Chem. B*, 2005, **109**, 22860.
16 M. V. Ganduglia-Pirovano, J. L. F. Da Silva and J. Sauer, *Phys. Rev. Lett.*, 2009, **102**, 026101.
17 M. Nolan, *Chem. Phys. Lett.*, 2010, **499**, 126.
18 S. Bedrane, C. Descorme and D. Duprez, *Catal. Today*, 2002, **401**, 75.
19 W. Li, F. J. Garcia and E. E. Wolf, *Catal. Today*, 2003, **81**, 437.
20 M. Nolan and G. W. Watson, *J. Phys. Chem. B*, 2006, **110**, 16600.
21 M. Nolan, S. C. Parker and G. W. Watson, *J. Phys. Chem. B*, 2006, **110**, 2256.
22 Z. X. Yang, T. K. Woo and K. Hermansson, *Surf. Sci.*, 2006, **600**, 4953.
23 D. R. Mullins and S. H. Overbury, *Surf. Sci.*, 2002, **511**, L293.
24 E. Aneggi, J. Llorca, M. Boaro and A. Trovarelli, *J. Catal.*, 2005, **234**, 88.
25 K. B. Zhou, X. Wang, X. M. Sun, Q. Peng and Y. D. Li, *J. Catal.*, 2005, **229**, 206.
26 Z. Yang, T. K. Woo and K. Hermansson, *J. Chem. Phys.*, 2006, **124**, 224701.
27 W. Y. Hernandez, M. A. Centeno, F. Romero-Sarria and J. A. Odriozola, *J. Phys. Chem. C*, 2009, **113**, 5629.
28 S. Imamura, T. Hiashihara, Y. Saito, H. Aritani, H. Kanai, Y. Matsumura and N. Tsuda, *Catal. Today*, 1999, **50**, 369.
29 H. P. Sun, X. P. Pan, G. W. Graham, H.-W. Jen, R. W. McCabe, S. Thevuthasan and C. H. F. Penden, *Appl. Phys. Lett.*, 2005, **87**, 2019150.
30 B. M. Reddy, P. Bharali, P. Saikia, A. Kahn, S. Loridant, M. Muhler and W. Gruenert, *J. Phys. Chem. C*, 2007, **111**, 1878.
31 R. Dziembaj, M. Molenda, L. Chmielarz, M. Drozdek, M. M. Zaitz, B. Dudek, A. Rafalska-Lasocha and Z. Piwowarska, *Catal. Lett.*, 2010, **135**, 68.
32 D. R. Ou, T. Mori, F. Ye, T. Kobayashi, J. Zuo, G. Auchterlonie and J. Drennan, *Appl. Phys. Lett.*, 2006, **89**, 171911.
33 G. Dutta, U. V. Waghmare, T. Baidya, M. S. Hegde, K. R. Priolkar and P. R. Sarode, *Catal. Lett.*, 2006, **108**, 165.
34 G. Dutta, U. V. Waghmare, T. Baidya, M. S. Hegde, K. R. Priolkar and P. R. Sarode, *Chem. Mater.*, 2006, **18**, 3249.
35 H. Kadowaki, N. Saito, H. Nishiyama and Y. Inoue, *Chem. Lett.*, 2007, **36**, 440.
36 Z.-P. Liu, S. J. Jenkins and D. A. King, *Phys. Rev. Lett.*, 2005, **94**, 196102.
37 C. Zhang, A. Michaelides, D. A. King and S. J. Jenkins, *J. Phys. Chem. C*, 2009, **113**, 6411.
38 M. Nolan, *J. Phys. Chem. C*, 2009, **113**, 2425.
39 H. Tanaka, R. Kaino, K. Okumura, T. Kizuka and K. Tomishige, *J. Catal.*, 2009, **268**, 1.
40 P. G. Savva and A. M. Efstathiou, *J. Catal.*, 2008, **257**, 324.
41 L. Jiang, M. Wei, X. Xu, Y. Lin, Z. Lue, J. Song and X. Duan, *Ind. Eng. Chem. Res.*, 2011, **50**, 4398.
42 X. Wang, J. Ni, B. Lin, R. Wang, J. Lin and K. Wei, *Catal. Commun.*, 2010, **12**, 251.
43 J. Chen, J. Zhu, C. Chen, Y. Zhan, Y. Cao, X. Lin and Q. Zheng, *Catal. Lett.*, 2009, **130**, 254.
44 I. Yeriskin and M. Nolan, *J. Phys.: Condens. Matter*, 2010, **22**, 135004.
45 W. Tang, Z. Hu, M. Wang, G. D. Stucky, H. Metiu and E. W. McFarland, *J. Catal.*, 2010, **273**, 125.
46 Z. Yang, G. Luo, Z. Lu and K. Hermansson, *J. Chem. Phys.*, 2007, **127**, 074704.
47 D. O. Scanlon, B. J. Morgan and G. W. Watson, *Phys. Chem. Chem. Phys.*, 2011, **13**, 4279.
48 X. Wang, M. Shen, J. Wang and S. Fabris, *J. Phys. Chem. C*, 2010, **114**, 10221.
49 V. I. Anisimov, J. Zaanen and O. K. Andersen, *Phys. Rev. B: Condens. Matter*, 1991, **44**, 943.
50 S. L. Dudarev, G. A. Botton, S. Y. Savrasov, C. J. Humphreys and A. P. Sutton, *Phys. Rev. B: Condens. Matter Mater. Phys.*, 1998, **57**, 1505.
51 B. G. Janesko, T. M. Henderson and G. E. Scuseria, *Phys. Chem. Chem. Phys.*, 2009, **11**, 443.
52 T. M. Henderson, J. Paier and G. E. Scuseria, *Phys. Status Solidi B*, 2010, DOI: 10.1002/pssb.201046303.
53 Y. Lykhach, T. Staudt, R. Streber, M. P. Lorenz, A. Bayer, H. P. Steinrück and J. Libuda, *Eur. Phys. J. B*, 2010, **75**, 89.
54 Y. Lykhach, T. Staudt, N. Tsud, T. Skala, K. C. Prince, V. Matolin and J. Libuda, *J. Phys. Chem. C*, 2011, **115**, 8716.
55 T. Staudt, Y. Lykhach, N. Tsud, T. Skala, K. C. Prince, V. Matolin and J. Libuda, *J. Catal.*, 2010, **275**, 181.
56 V. Matolin, J. Libra, I. Matolinova, V. Nehasil, L. Sedlacek and F. Sutara, *Appl. Surf. Sci.*, 2007, **254**, 153.
57 T. Staudt, Y. Lykhach, L. Hammer, M. A. Schneider, V. Matolin and J. Libuda, *Surf. Sci.*, 2009, **603**, 3382.
58 D. R. Mullins, S. H. Overbury and D. R. Huntley, *Surf. Sci.*, 1998, **409**, 307.
59 N. Yi, R. Si, H. Saltsburg and M. Flytzani-Stephanopolous, *Appl. Catal., B*, 2010, **95**, 87.
60 F. Šutara, M. Cabala, L. Sedláček, T. Skála, M. Škoda, V. Matolín, K. C. Prince and V. Cháb, *Thin Solid Films*, 2008, **516**, 6120.
61 G. Kresse and J. Hafner, *Phys. Rev. B: Condens. Matter*, 1994, **49**, 14251; G. Kresse and J. Furthmüller, *Comput. Mater. Sci.*, 1996, **6**, 15.
62 P. E. Blöchl, *Phys. Rev. B: Condens. Matter*, 1994, **50**, 17953; D. Joubert and G. Kresse, *Phys. Rev. B: Condens. Matter Mater. Phys.*, 1999, **59**, 1758.
63 J. P. Perdew, K. Burke and M. Ernzerhof, *Phys. Rev. Lett.*, 1996, **77**, 3865.
64 P. W. Tasker, *J. Phys. C*, 1980, **6**, 488.

65 M. Nolan, *J. Mater. Chem.*, 2011, **21**, 9160.
66 V. I. Anisimov, J. Zaanen and O. K. Andersen, *Phys. Rev. B: Condens. Matter*, 1991, **44**, 943.
67 J. L. F. Da Silva, M. V. Ganduglia-Pirovano, J. Sauer, V. Bayer and G. Kresse, *Phys. Rev. B: Condens. Matter Mater. Phys.*, 2007, **75**, 045121.
68 P. J. Hay, R. L. Martin, J. Uddin and G. E. Scuseria, *J. Chem. Phys.*, 2006, **125**, 34712.
69 V. Matolín, I. Matolínová, L. Sedláček, K. C. Prince and T. Skála, *Nanotechnology*, 2009, **20**, 215706.
70 D. R. Mullins, S. H. Overbury and D. R. Huntley, *Surf. Sci.*, 1998, **409**, 307.
71 Y. Bouvier, B. Mutel and J. Grimblot, *Surf. Coat. Technol.*, 2004, **180–181**, 169.
72 MSIT®. N. Bochvar, O. Fabrichnaya, Y. Liberov, Ce–Mg–O (Cerium–Magnesium–Oxygen), , in *Non-Ferrous Metal Ternary Systems. Selected Nuclear Materials and Engineering Systems: Phase Diagrams, Crystallographic and Thermodynamic Data*, ed. G. Effenberg and S. Ilyenko, Springer Materials–The Landolt-Börnstein Database, vol. 11C4: Non-Ferrous Metal Systems. Part 4.
73 M. Chen, H. Zheng, C. M. Shi, R. X. Zhou and X. M. Zheng, *J. Mol. Catal. A: Chem.*, 2005, **237**, 132.
74 J. F. Chen, J. J. Zhu, Y. Y. Zhan, X. Y. Lin, G. H. Cai, K. M. Wei and Q. Zheng, *Appl. Catal., A*, 2009, **363**, 208.
75 W. S. M. Werner, W. Smekal and C. J. Powell, *NIST Database for the Simulation of Electron Spectra for Surface Analysis–Version 1.1*, National Institute of Standards and Technology, Gaithersburg, MD, 2006.